



Article

Experimental Study on Thermal Performance of a Loop Heat Pipe with Different Working Wick Materials

Kyaw Zin Htoo ¹, Phuoc Hien Huynh ², Keishi Kariya ³ and Akio Miyara ^{3,4,*}

¹ Graduate School of Science and Engineering, Saga University, 1 Honjo-machi, Saga 840-8502, Japan; 18694903@edu.cc.saga-u.ac.jp

² Department of Heat and Refrigeration Engineering, Ho Chi Minh City University of Technology—VNU—HCM (HCMUT), 268 Ly Thuong Kiet, Ho Chi Minh City 72409, Vietnam; hphien@hcmut.edu.vn

³ Department of Mechanical Engineering, Saga University, 1 Honjo-machi, Saga 840-8502, Japan; kariya@me.saga-u.ac.jp

⁴ International Institute for Carbon-Neutral Energy Research, Kyushu University, Nishi-ku, Motooka, Fukuoka 819-0395, Japan

* Correspondence: miyara@me.saga-u.ac.jp

Abstract: In loop heat pipes (LHPs), wick materials and their structures are important in achieving continuous heat transfer with a favorable distribution of the working fluid. This article introduces the characteristics of loop heat pipes with different wicks: (i) sintered stainless steel and (ii) ceramic. The evaporator has a flat-rectangular assembly under gravity-assisted conditions. Water was used as a working fluid, and the performance of the LHP was analyzed in terms of temperatures at different locations of the LHP and thermal resistance. As to the results, a stable operation can be maintained in the range of 50 to 520 W for the LHP with the stainless-steel wick, matching the desired limited temperature for electronics of 85 °C at the heater surface at 350 W (129.6 kW·m⁻²). Results using the ceramic wick showed that a heater surface temperature of below 85 °C could be obtained when operating at 54 W (20 kW·m⁻²).

Keywords: electronics cooling; loop heat pipe; wick materials; thermal conductivity



Citation: Htoo, K.Z.; Huynh, P.H.; Kariya, K.; Miyara, A. Experimental Study on Thermal Performance of a Loop Heat Pipe with Different Working Wick Materials. *Energies* **2021**, *14*, 2453. <https://doi.org/10.3390/en14092453>

Academic Editors: Alessandro Mauro and Gabriela Huminc

Received: 1 March 2021

Accepted: 20 April 2021

Published: 25 April 2021

Publisher's Note: MDPI stays neutral with regard to jurisdictional claims in published maps and institutional affiliations.



Copyright: © 2021 by the authors. Licensee MDPI, Basel, Switzerland. This article is an open access article distributed under the terms and conditions of the Creative Commons Attribution (CC BY) license (<https://creativecommons.org/licenses/by/4.0/>).

1. Introduction

Loop heat pipes use a passive two-phase heat transport device in which advantageous characteristics are offered, such as operation against the gravity through the capillary effect and flexible characteristics. They have been widely used in energy applications, spacecraft thermal control, electronic device cooling, and commercial radiators [1]. Zhou [2] fabricated a plate-type loop heat pipe (LHP) and investigated the effect on the heat transfer performance of the LHP with multilayer metal foams as a wick structure. Their flat evaporator's experimental results show that multilayer copper foams have better performance than nickel foam because of higher thermal conductivity and smaller pore size. Siedel [3] presented a numerical simulation, comparing it with the experimental data of a flat disk-shaped evaporator. The results showed that the larger effective thermal conductivity of wick has an influence on the overall thermal performance of the LHP. However, other researchers, Maydanik [4] and Hoang [5], suggested the wick material, with its lower effective thermal conductivity, to handle the problem of heat leakage. In addition, the hydrophilic effect on the ceramic wick structure is higher than that of stainless steel [6]. Therefore, the performances of stainless-steel wicks and ceramic wicks in LHPs are compared in this study, of which the ceramic wick has much lower thermal conductivity and a higher hydrophilic effect [7,8]. In an LHP system, the porous wicks' structure is essential because it provides the capillary force for working fluid circulations, a liquid flow path, and a place for phase change heat transfer. Moreover, the porosity effect of the wick materials inside the evaporator is necessarily considered for improving the overall performance of

LHPs [9]. Therefore, the porosity, pore diameter, and thermal conductivity of the wicks were measured. The influence of the different wicks on the performance of LHPs is tested with the designed evaporator. Although this is a simple case study of an arrangement with different wicks, the appropriate engineering approach of the calculation procedure related to applying the designed evaporator is presented in this paper. It may improve the understanding of the problems that exist in the LHP evaporator and future LHP systems.

The LHP has some similar operation principles with conventional HPs. The phase changing process is happened in the LHP system and the capillary force is used as the motivation for the operation. Figure 1 demonstrates the scheme of the analytical LHP and an operation cycle diagram.

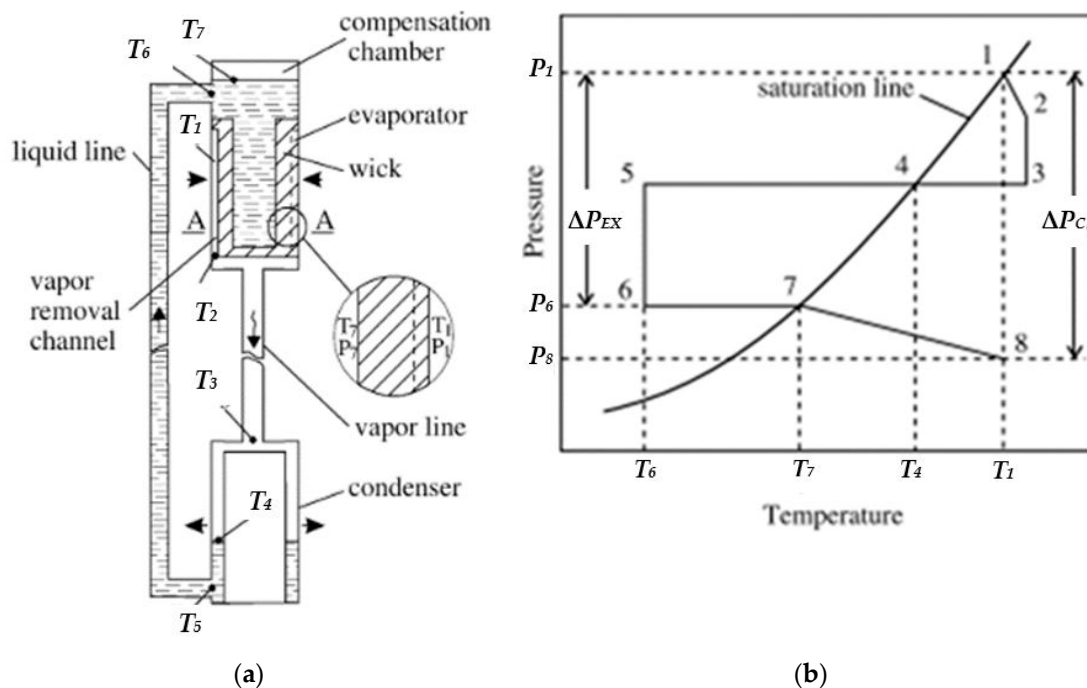


Figure 1. Principles of LHP: (a) Scheme of analytical LHP. (b) LHP working cycle diagram. Reproduced from [1], Yu.F.Maydanik: 2005.

At first, the system is not supplied with heat load. In this case, the liquid stays at Level A–A as an assumption. The liquid found at the evaporator zone (Point 1) and the compensation chamber evaporates from the wick when heat is supplied to the evaporator. The vapor from the evaporator flows. Then, it approaches to the heating wall. As a result, the vapor pressure reduces. Simultaneously, the temperature rises a little (Point 2) and is higher than the vapor located at the compensation chamber. In this situation, the wick behaves as a thermal barrier. The vapor which is superheated condition in the evaporator zone cannot pass the compensation chamber through the wick which is saturated due to the force of capillary that keeps the liquid inside. Then, the hydraulic lock is happened in the wick. Afterwards, the vapor continuously flow to the condenser's inlet (Point 3). When vapor flows from Point 2 to Point 3, both temperature and pressure decrease. The de-superheat, condensation, and subcooled processes happen from Point 3 to Point 5. In this case, there is no pressure loss from Point 3 to Point 5 as an assumption. Because of the pressure loss and the hydrostatic resistance caused by friction, the pressure difference ΔP_{56} includes the pressure loss. Afterward, the liquid located at Stage 6 flows into the chamber for compensation. Moreover, some parts of the heat load are provided to the evaporator at the expense of the working fluid. This condition is heated to temperature T_7 . The progress from Point 7 and Point 8 are relative to the filtration of the liquid through the wick into the evaporation place. In this way, the liquid may prove to be superheated. However, its boiling-up does not happen because of its short duration in such a state. The state of the working fluid in the vicinity of the evaporating menisci is represented by Point 8.

Pressure loss (dP_{1-8}) corresponds to the total value of pressure losses in all the working-fluid circulation sections. From the above analysis, the function of the LHP is considered in three conditions. At first, the capillary condition is the condition for conventional HPs for an operation.

$$\Delta P_c \geq \Delta P_v + \Delta P_l + \Delta P_g \quad (1)$$

where

ΔP_v is the working fluid's pressure loss during the vapor state's motion.

ΔP_l is the working fluid's pressure loss during the liquid state's motion.

ΔP_g is the pressure loss because of the hydrostatic of the liquid column.

ΔP_c is the wick capillary pressure.

The second condition is just for the LHP. At the LHP's startup, it ensures that the liquid is exhibited from the evaporating zone to the compensation chamber.

$$\left. \frac{\partial P}{\partial T} \right|_{T_v} \Delta T_{1-7} = \Delta P_{EX} \quad (2)$$

where

$\partial P/\partial T$ is the derivative of the saturated line's slope. T_v is the mean temperature between T_1 and T_7 .

ΔP_{EX} is the total pressure loss in all the sections of the working fluid's circulation except the wick.

At the third condition, the liquid is prevented from steaming in the liquid line because of the ambient pressure loss and heating.

$$\left. \frac{\partial P}{\partial T} \right|_{T_v} \Delta T_{4-5} = \Delta P_{5-6} \quad (3)$$

where

$\partial P/\partial T$ is the derivative of the saturation line's slope. T_v is the mean temperature between T_4 and T_5 .

ΔP_{5-6} is the pressure loss in total from State 5 to State 6.

The working fluid should own a high value of dP/dT to minimize the temperature difference ΔP_{1-7} and ΔP_{4-6} from the second condition.

The purpose of the tested LHP in this study is the cooling of electronics such as processors located at Data Centers (DCs). Therefore, the evaporator surface which is heated needs to be flat to improve the evaporator and electronics' contact quality. Moreover, it will make the heat flux q and distribution of temperature on the active surfaces uniform and eliminate the occurrence of mounting blocks at the evaporator. The investigated evaporator design belongs to the evaporator group with opposite replenishment (EOA). In this design, liquid flows from the top to the bottom surface of the wick structure, as shown in Figure 2a. Figure 2b shows the evaporator with longitudinal replenishment (ELR). The liquid from ELR is provided from the compensation chamber which is located behind the wick. Otherwise, the liquid flows perpendicular to the heat flow rate. The evaporator with opposite replenishment own a simple structure and the liquid absorption surface is large. However, the evaporator can become thicker because the compensation chamber is located above the capillary system. Moreover, the heat leak from the evaporator to the compensation chamber through the wick will be more severe because of the large cross-section of the wick.

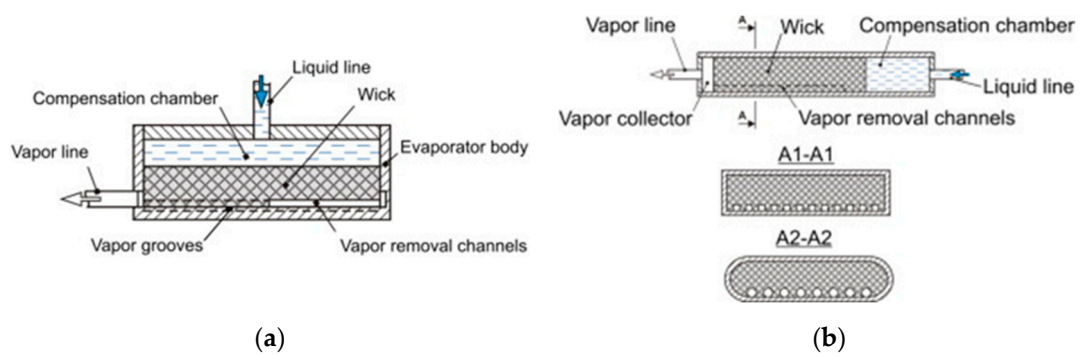


Figure 2. LHP evaporators (a) Opposite replenishment, (b) Longitudinal replenishment. Reproduced from [10], Y.F. Maydanik: 2014.

The investigated evaporator has two parts: the vapor collector and the wick's space and compensation chamber. The copper plate is used for the separation between two elements. The brazing method is used to fix them. Additionally, to install the thermocouples, a hole with a 1-mm diameter and 22.5 mm for the length was fabricated at the evaporator's base. The heating block's top surface and the evaporator's bottom surface have the same area: 27 cm^2 ($45 \times 60 \text{ mm}$). This dimension was considered based upon the specifications of some processors, as presented in Table 1. Different LHP technologies focussing on various designs of the LHP's evaporator and other types of LHPs such as miniature LHPs, micro LHPs, evaporator with longitudinal replenishment (ELR) LHPs, and LHPs with parallel condensers are compared and summarized in Table 2.

Table 1. Processor specifications.

No.	Modern	Thermal Power Design (W)	Case Dimensions (mm × mm)	Heat Flux (W/cm ²)
1	Core i7 5960X	140	52.5 × 45	5.9
2	Core i7 5930K	140	52.5 × 45	5.9
3	Core i7 4960X	130	52.5 × 45	5.48
4	Core i7 4930X	130	52.5 × 45	5.48
6	Core i7 3790X	150	52.5 × 45	6.3
7	Xeon E7 8891 v3	165	52 × 45	7.05
8	Xeon E7 8880 v3	150	52 × 45	6.41
9	Xeon E7 8890 v2	155	52 × 45	6.62
10	Itanium 9300	185/155/130	48.5 × 40.25	9.47/7.94/6.66
11	Itanium 9500	170/130	48.5 × 40.25	8.71/6.66

Table 2. Different LHP technologies from the literature.

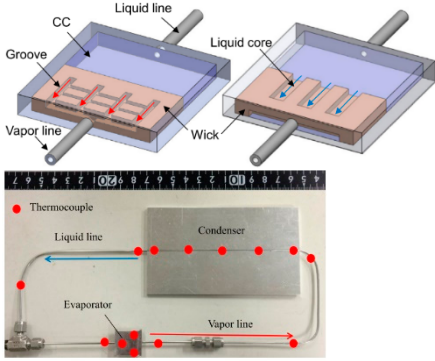
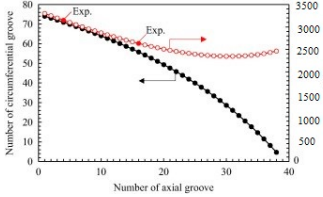
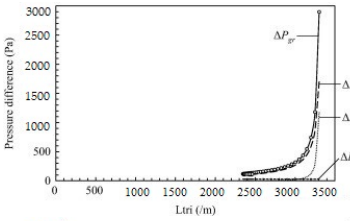
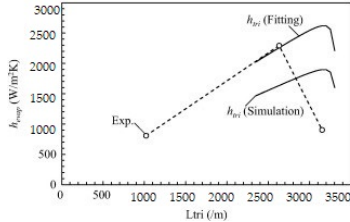
No.	References	Specifications of LHPs from the Literature	Objects and Results
1.	<p>K. Fukushima—2017 [11] Keywords: Capillary force, heat transport, LHP, porous PTFE</p>	<p>Flat—rectangular evaporator New-fashioned flat evaporator structure, micro-LHP (Evaporator $20 \times 10 \times 3$ mm, 200 mm in length transport line) Porous polytetrafluorethylene wick $17 \times 9 \times 2$ mm (PTFE) (50%, $2.2 \mu\text{m}$, 6.48×10^{-14} m², 0.25 W/m·K) Working fluid: ethanol.</p>	<p>Objects: A wick with a liquid core is proposed. An experimental and computational investigation was conducted. The temperature distribution inside the evaporator and the heat load's break down from the mathematical model are obtained. Results: Minimum R_{LHP} is 1.2 K/W and maximum $Q = 11$ W, from the experiment.</p>
2.	<p>M. Nishikawara—2017 [12] Keywords: Capillary evaporator, capillary pumped loop, evaporator HTC, LHP, optimized wick shape, 3-phase contact line</p>	<p>PTFE wick (bulk thermal conductivity = 0.25 W/m·K). Stainless steel case ($k = 16$ W/m·K) Machined widths (minimum): 0.3 (circumferential groove) and 0.4 mm (axial groove)</p> <p>Increasing axial grooves will reduce the number of circumferential grooves. Three wicks were fabricated for experimental examination: $L_{tri} = 3150$ m (4 axial \times 71 circumferential) $L_{tri} = 2630$ m (16 axial \times 56 circumferential) Classical wick with only 16 axial grooves and 1 mm width of the groove</p>	<p>Objects: It presents a method for the wick shape optimization via calculation and experiment. Using only the three-phase contact line's length, the h_{evap} is maximized ($q = 2$ W/cm²). Effects of the case, wick material, and the working fluid, are discussed. Results: The effect of the three-phase contact line (TPCL) on the groove pressure loss (by calculation) is shown. Comparison between evaporator heat-transfer coefficient (HTC) obtained using Equation (9) and that obtained through the experiments (ethanol) is presented.</p>     <p>The heat transport's contribution at TPCL was estimated at 0.87 when fitting to experiment results and 0.63 in simulation. Comparison of various working fluids and wick materials, h_{tri} increased with wick's thermal conductivity. The value of h_{tri} was higher for ammonia due to the changes in interfacial HTC.</p>

Table 2. Cont.






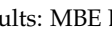
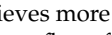





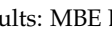
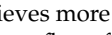





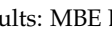
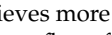
No.	References	Specifications of LHPs from the Literature	Objects and Results																																
3.	Jinliang Xu—2014 [13] Keywords: LHP, evaporator, heat transfer, modulated porous wick	Flat-disk shape evaporator. Tilt angles: -90° , -60° , -30° , 0° , 90° (“-”: antigravity) Forced convective air cooling ($T_a = 22$ to 24°C) Water as working fluid There are three layers of porous materials, primary layer (as shown in table), secondary copper table ($2\text{ mm}-149\mu\text{m}$), and third absorbent wool layer ($2\text{ mm}-r_{\text{pore}} = 20\mu\text{m}$) Evaporator: $\phi 80 \times 10$ (without CC thickness); $A_{\text{heating}} = 5\text{ cm}^2$ Vapor line: $ID6/OD8 \times 550\text{ mm}$ Liquid line: $ID6/OD8 \times 300\text{ mm}$ Condenser: $130 \times 130 \times 25$ $CR = 38.5\%$, 51.3% ; 64.1% , 64.1% , 76.9% Sintering process: oven temperature 900°C for 4 h.	<p>Objects: It is to enhance heat transfer of pool boiling using the modulated porous wick sintered on the heater wall. Three types of evaporators: MWE (microchannel/wick evaporator), MME (modulated monoporous wick evaporator), and MBE (modulated biporous wick evaporator) were fabricated.</p> <p>The structure adjacent to the evaporator wall.</p> <table border="1" data-bbox="906 593 1476 817"> <thead> <tr> <th>Run</th> <th>Schematic drawing of the structure adjacent to the evaporator wall</th> <th>Structure parameter (mm)</th> <th>Evaporator type and particle size (μm)</th> </tr> </thead> <tbody> <tr> <td>1</td> <td></td> <td>$h=1.5, p=1.5, w=3.0$</td> <td>MWE, the porous wick is above microchannels</td> </tr> <tr> <td>2</td> <td></td> <td>$h=1.5, p=1.0, w=3.0$</td> <td>MME: 88 (78-92)</td> </tr> <tr> <td>3</td> <td></td> <td>$h=1.5, p=1.5, w=2.0$</td> <td>MME: 88 (78-92)</td> </tr> <tr> <td>4</td> <td></td> <td>$h=1.5, p=1.5, w=3.0$</td> <td>MME: 37 (25-42) MME: 88 (78-92)</td> </tr> <tr> <td>5</td> <td></td> <td>$h=1.5, p=1.5, w=4.0$</td> <td>MME: 149 (75-154)</td> </tr> <tr> <td>6</td> <td></td> <td>$h=1.5, p=2.0, w=3.0$</td> <td>MME: 88 (78-92)</td> </tr> <tr> <td>7</td> <td></td> <td>$h=2.0, p=2.0, w=3.0$</td> <td>MME: 88 (78-92)</td> </tr> </tbody> </table> <p>Results: MBE LHP reduces the startup time and achieves more stable operation than MWE. At heat flux of 40 W/cm^2 (heater heat flux), the MBE LHP can operate when T_c is around 63°C; ($R_t = 0.12\text{ K/W}$) Optimum CR = 51.3%. Operation antigravity condition is better than others with the MBE LHP’s proper design. Best fin’s geometric parameters: $h = 1.5\text{ mm}$; $p = 1.5\text{ mm}$; $w = 3\text{ mm}$; best particle size: $88\mu\text{m}$</p>	Run	Schematic drawing of the structure adjacent to the evaporator wall	Structure parameter (mm)	Evaporator type and particle size (μm)	1		$h=1.5, p=1.5, w=3.0$	MWE, the porous wick is above microchannels	2		$h=1.5, p=1.0, w=3.0$	MME: 88 (78-92)	3		$h=1.5, p=1.5, w=2.0$	MME: 88 (78-92)	4		$h=1.5, p=1.5, w=3.0$	MME: 37 (25-42) MME: 88 (78-92)	5		$h=1.5, p=1.5, w=4.0$	MME: 149 (75-154)	6		$h=1.5, p=2.0, w=3.0$	MME: 88 (78-92)	7		$h=2.0, p=2.0, w=3.0$	MME: 88 (78-92)
Run	Schematic drawing of the structure adjacent to the evaporator wall	Structure parameter (mm)	Evaporator type and particle size (μm)																																
1		$h=1.5, p=1.5, w=3.0$	MWE, the porous wick is above microchannels																																
2		$h=1.5, p=1.0, w=3.0$	MME: 88 (78-92)																																
3		$h=1.5, p=1.5, w=2.0$	MME: 88 (78-92)																																
4		$h=1.5, p=1.5, w=3.0$	MME: 37 (25-42) MME: 88 (78-92)																																
5		$h=1.5, p=1.5, w=4.0$	MME: 149 (75-154)																																
6		$h=1.5, p=2.0, w=3.0$	MME: 88 (78-92)																																
7		$h=2.0, p=2.0, w=3.0$	MME: 88 (78-92)																																
4.	S.C. Wu—2014 [14] Keywords: Wick structure, LHP, evaporator area, grooves	LHP with cylindrical stainless-steel evaporator ($\phi 16 \times 65$) Water cooling Wick material: nickel ($ID/OD = 9/12.5$); largest $r_{\text{pore}} = 1.9 - 2.5\mu\text{m}$; $K = 1.3 - 3.25 \times 10^{-13}\text{ m}^2$, porosity: 63–67%. Vapor line: $ID5/OD6 \times 470$ Liquid line: $ID4.5/OD6 \times 585$ Condenser: $ID5/OD6.4 \times 800$ Ammonia as working fluid.	<p>Objects: The effects of increasing the number of grooves on a wick’s surface on LHP performance were investigated.</p> <table border="1" data-bbox="906 1211 1289 1458"> <tbody> <tr> <td>(a) A_9</td> <td>(b) A_8</td> <td>(c) A_{10} $A_{a10} = 25\%$</td> </tr> <tr> <td>(d) A_{12} $A_{a12} = 50\%$</td> <td>(e) A_{14} $A_{a14} = 75\%$</td> <td>(f) A_{16} $A_{a16} = 100\%$</td> </tr> </tbody> </table> <p>Results: The wick with 16-groove was quickly damage. The other wicks have similar properties, such as porosity, pore radius, K. Sintering condition: 45 min at 600°C. Increasing the groove number increases the LHP’s performance ($Q = 500\text{ W}$, $R_t = 0.14\text{ K/W}$). An optimal number of grooves fabricated on the wick surface is presented.</p>	(a) A_9	(b) A_8	(c) A_{10} $A_{a10} = 25\%$	(d) A_{12} $A_{a12} = 50\%$	(e) A_{14} $A_{a14} = 75\%$	(f) A_{16} $A_{a16} = 100\%$																										
(a) A_9	(b) A_8	(c) A_{10} $A_{a10} = 25\%$																																	
(d) A_{12} $A_{a12} = 50\%$	(e) A_{14} $A_{a14} = 75\%$	(f) A_{16} $A_{a16} = 100\%$																																	

Table 2. Cont.

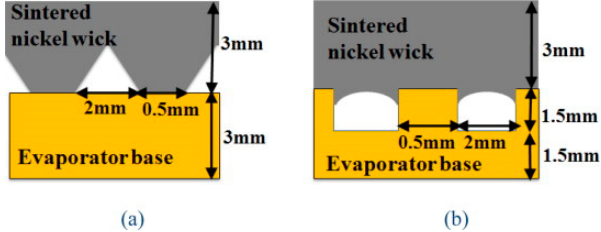
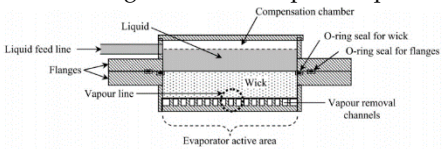
No.	References	Specifications of LHPs from the Literature	Objects and Results
5.	Jeehoon Choi—2013 [15] Keywords: Miniature LHP, evaporator, sintering, contact conductance, thermal resistance	Flat-disk shape evaporator. Wick material = Nickel ($\phi 42 \times 3$), particles size: $3 \mu\text{m}$, $P_{\text{capillary}} = 401 \text{ kPa}$, $K = 0.99 \cdot 10^{-11} \text{ m}^2$, porosity = 64%, $k_{\text{eff}} = 9 \text{ W/K}\cdot\text{m}$ CC: stainless-steel ($\phi 46 \times 7$) Vapor line: $ID4.95/OD6.35 \times 250$ (made by copper) Liquid line: $ID4.95/OD6.35 \times 300$ (made by stainless-steel) Forced convective air cooling Working fluid: water Horizontal orientation Heater surface area: $30 \times 30 \text{ mm}^2$	<p>Objects: For fabricating the LHP's evaporator, a low-cost sintering method is explored. The porous material partially fills the vapor collection channel embedded in the evaporator's base; two evaporators were fabricated.</p>  <p>(a) (b)</p> <p>A sintering procedure is used to fabricate the evaporator shown in Figure (b). It is presented in Section 2.2 of the paper.</p> <p>Results: The startup of LHP with the second evaporator was shorter in time and more stable than one with the traditional LHP. By using the evaporator with the interpenetrated wick, the temperature on the CC reduced significantly which is $34 \text{ }^\circ\text{C}$. Traditional LHP operated at $30\text{--}165 \text{ W}$; $80\text{--}141 \text{ }^\circ\text{C}$; $1.81\text{--}0.71 \text{ K/W}$ LHP using interpenetrated wick/base plate: $30\text{--}180 \text{ W}$; $47\text{--}102 \text{ }^\circ\text{C}$; $0.76\text{--}0.43 \text{ K/W}$ The lower temperature of the CC was due to the design of the second evaporator. It helped the wick and evaporator base contact excellently. It reduced heat loss to the CC through the evaporator's wall.</p>
6.	Randeep Singh—2008 [16] Keywords: LHP, heat transfer, thermal performance, miniature LHP, flat evaporator, thermal control	Miniature LHP using flat disk-shaped copper evaporator ($\phi 30 \times 10 \text{ mm}$) Working fluid: water Nickel wick (thickness = 3 mm , $r_{\text{pore}} = 3\text{--}5 \mu\text{m}$; porosity: 75%) Condenser using Air forced cooling ($T_a = 22 \pm 2 \text{ }^\circ\text{C}$) Copper Vapor line: $\phi 2 \times 150 \text{ mm}$ Copper Liquid line: $\phi 2 \times 290 \text{ mm}$ Heater surface area: $25 \times 25 \text{ mm}$ Condenser: $\phi 2 \times 50 \text{ mm}$	<p>Objects: For the thermal control of small electronic equipment, it addresses the thermal characteristics of mLHP using a flat disk-shaped evaporator.</p>  <p>Results: Startup condition at different heat loads, $Q = 5\text{--}70 \text{ W}$, $R_{\text{mLHP}} = 5.66\text{--}0.17 \text{ K/W}$. The evaporator wall's temperature was lower than $100 \text{ }^\circ\text{C}$. Oscillating behavior was found when Q was between 10 and 20 W. This oscillation occurred due to the fluctuation of heat loss from the evaporator to the CC and the subcooled liquid temperature.</p>

Table 2. Cont.

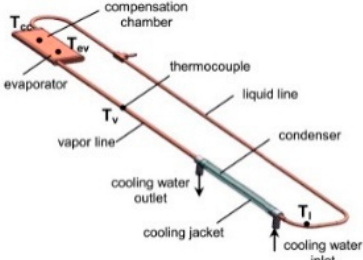
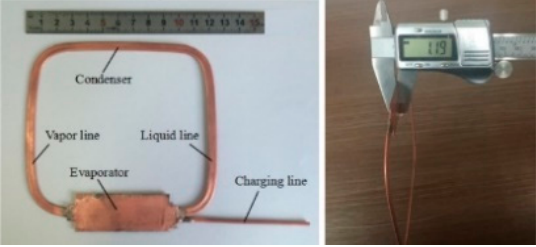
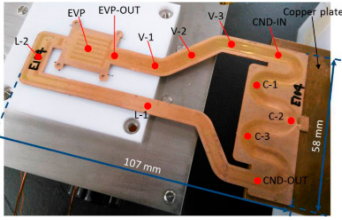

No.	References	Specifications of LHPs from the Literature	Objects and Results
7.	M.A. Chernysheva—2014 [17] Keywords: LHP, supercomputer, cooling system, operating temperature, thermal resistance	Flat-oval evaporator (longitudinal replenishment evaporator) $80 \times 42 \times 7$ mm, $A_{active} = 32 \times 42$ mm ² 12 Vapor grooves $\phi 1.8 \times 33$ Copper wick (porosity 43%, $r_{pore} = 27$ μ m) Vapor line: (1) $ID4/OD5 \times 305$ mm, (2) $ID3/OD4 \times 305$ mm Liquid line: $ID3/OD4 \times 810$ mm Condenser: $ID4/OD5 \times 160$ mm	<p>Objects: A cooling system with an LHP for a supercomputer's thermal control is presented. Copper loop heat pipes with different vapor pipe IDs (4 and 3 mm each) were fabricated. The test was carried out with a heat load from 20 to 600 W during the cooling water's temperature was changed from 20 to 80 °C.</p>  <p>Results: LHP's operating temperature varied slightly when the condenser cooling temperature changed in the range below 40 °C (called as variable conductance mode). It is more applicable to use copper-water LHPs when cooling temperatures of condenser is above 50 °C.</p>
8.	Guohui Zhou—2016 [18] Keywords: Miniature LHP, ultrathin, thermal resistance, mobile electronics	Flat evaporator (thickness, $\delta = 1.2$ mm), vapor line, liquid line, and condenser line ($\delta = 1$ mm) Evaporator: $60 \times 23 \times 1.2$ mm A_{active} : 15×9 mm Primary porous material (inside evaporator): sintered from 10 layers of 500 mesh copper wire mesh (porosity: 65.2%) Secondary wick (in liquid line) sintered from 4 layers of 150 mesh copper wire mesh ($\delta = 0.43$ mm) Liquid line: 105 mm, vapor line: 105 mm. Condenser: 125 mm (Natural cooling) LHP's inclination: horizontal, anti-, and assisted gravity. Water as working fluid	<p>Objects: mLHP for mobile electronics.</p>  <p>Results: Startup of LHP happened at 2 W with evaporator temperature 43.9 °C. When Q is at 11 W, $R_{LHP} = 0.11$ K/W. There is no noticeably different performance with different orientations. For cooling mobile electronics: a tablet or smartphone, this mLHP achieves a promising thermal management solution.</p>

Table 2. Cont.

No.	References	Specifications of LHPs from the Literature	Objects and Results
9.	Takeshi Shioga—2015 [19] Keywords: Micro LHP, thermal resistance, heat leak, operation orientation	Micro loop heat pipe Chemical-etching and diffusion bonding process for fabrication Evaporator: $20 \times 17 \times 0.6$ mm Vapor line: (1) 5.6×0.4 and (2) 1×75 mm in length Liquid line $4 \times 0.4 \times 120$ mm Condenser (1) 5.6×0.4 and (2) 1×110 mm in length Working fluid: water	<p>Objects: This micro LHP was fabricated for mobile electronic devices. The effect of vapor and condenser thickness on μLHP performance was investigated.</p>  <p>Results: The μLHP could not operate with vapor line and condenser line thickness at 0.4 mm. When Q is at 5 W, $R_{LHP} = 0.8$ K/W, $T_{evaporator} = 50.5$ °C. When $Q = 15$ W, $R_{LHP} = 0.32$ K/W. Heat loss was estimated at around 11%. Based on the operating orientation, the LHP's performance was slightly changed.</p>
10.	Ji Li—2013 [20] Keywords: LED cooling, LHP, parallel condensers, thermal resistance	Evaporator: $30 \times 30 \times 15$ (in mm). Gravity assisted LHP Connecting line: ID 5 mm Wick material is copper (porosity 50%, $r_{pore} = 65$ μ m, $K = 6 \times 10^{-11}$ m ²) $A_{Heater} = 25 \times 25$ mm ² Condenser size: $120 \times 80 \times 50$ mm	<p>Objects: The investigation of copper-water LHP using dual parallel condensers was conducted primarily for LED illumination applications with high-power.</p>  <p>Results: At $Q = 300$ W, the value of R is 0.4 °C/W; with $T_{air} = 15$ °C, $Q = 0$–100 W, $T_{junction} < 75$ °C. At low heat loads, the condenser's unpredictable nonuniform performance caused the unstable behavior of the LHP.</p>

2. Experimental Setups and Data Reduction

2.1. Description of Test LHP

The elevation difference between the evaporator and condenser is 350 mm in this experiment. Cartridge heaters were used and inserted into the copper heating block at the evaporator base. The heat is rejected at the water-cooled condenser. The mass flow rate and inlet temperature of cooling water were around 7.5×10^{-3} kg s⁻¹ and 27.5 °C, respectively. The power supplied to the evaporator was adjusted and measured by a volt slider and a digital power meter, respectively. The thermal contact resistance between the heating block and the evaporator is minimized by thermal grease, which was filled in the interface and fixed with screws. Pressure transducers and four thermocouples were inserted directly into the path of the working fluid at different positions of the LHP, such as at evaporator outlet T_{eo} , condenser inlet T_{ci} , condenser outlet T_{co} , and the inlet of compensation chamber T_{cci} . These temperature transducers detect the temperature distribution inside the LHP. Therefore, the characteristics of circulation, as well as phase distribution, can be evaluated. Pressure transducer P_e was installed at the outlet of the evaporator. Figures 3 and 4 and Table 3 show the schematic diagram, photo of the real experimental setup, and the main specifications of the LHP.

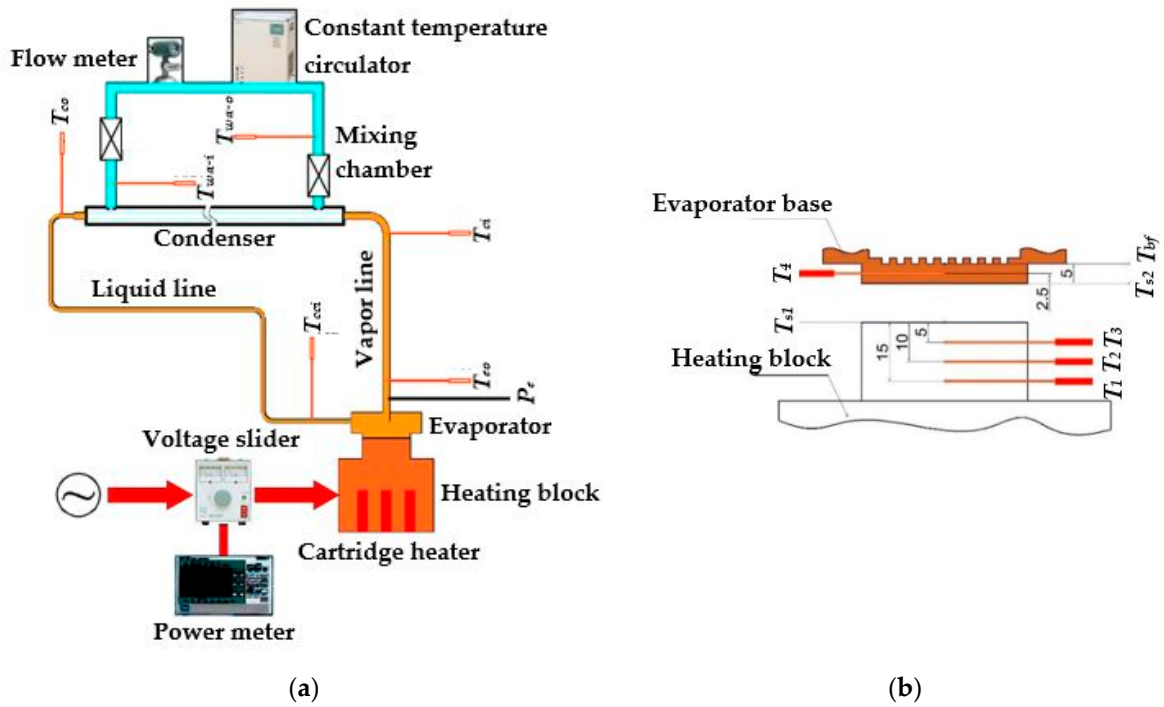


Figure 3. Test LHP: (a) Schematic diagram of the LHP and temperature measurement points. (b) The locations of thermocouples on heating block and evaporator.

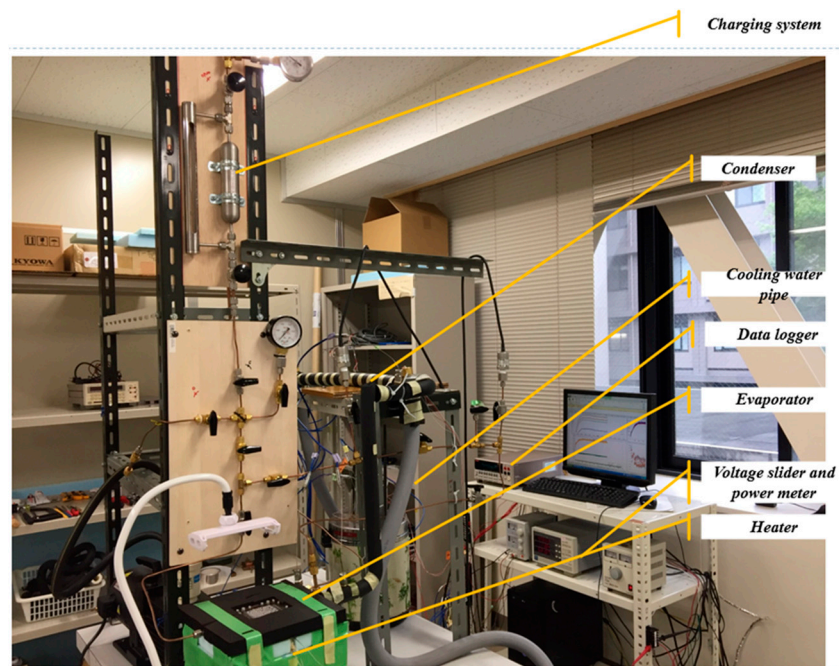


Figure 4. Photograph of the real experimental setup under gravity-assisted conditions.

Table 3. Main parameters of the LHP.

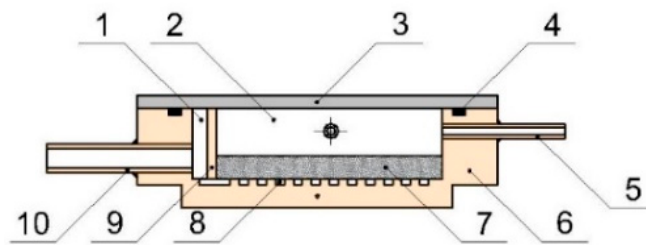
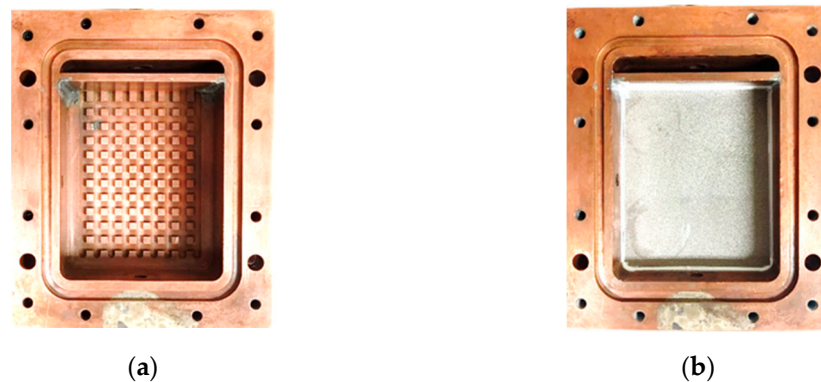
Evaporator Body	Values
Material	Copper
Length (mm)	80
Width (mm)	70
Height (mm)	24.5
Active area (mm ²)	60 × 45
Fin geometry	
Cross area (mm ²)	2 × 2
Height (mm)	1.5
Fin pitch (mm)	4
Wick structure	
Material	Stainless steel
Bulk volume (mm ³)	50 × 41 × 5
Material	Ceramic
Bulk volume (mm ³)	50 × 41 × 5
Vapor line	
OD/ID (mm)	6.35/4.35
Length (mm)	800
Condenser line	
OD/ID (mm)	6.35/4.35
Length (mm)	600
Liquid line	
OD/ID (mm)	3.2/1.7
Length (mm)	1300
Working fluid	
Water	
Amount (mL)	33

Thermocouples T_1 , T_2 , T_3 were installed, as shown in Figure 3b, to consider the temperature gradient caused by the heat flux and the temperature on the top surface of heating block T_{s1} , and the correct values of heating power and heat flux supplied to the evaporator were accessed. In the evaporator base, thermocouple T_4 was inserted to estimate the temperature at the evaporator's bottom surface; T_{s2} measures the temperature at the base of fin T_{bf} . The heat released from the condenser, Q_c , is obtained from the temperature difference of cooling water T_{wa-i} , T_{wa-o} , and the mass flow rate of cooling water. All measured data were collected and recorded by the KEITHLEY 2701 data acquisition system. Moreover, the level of liquid inside the compensation chamber can be observed by the polycarbonate evaporator cover.

Table 4 describes the uncertainties of the mass flow meter and thermocouples (obtained from the calibration process in which a Pt100 thermometer (Chino Co. Model—R900-F25AT) was used as the standard source). Figures 5 and 6 demonstrate the structure of the evaporator and the geometry of the evaporator's inner surface.

Table 4. Uncertainty values.

Parameters	Uncertainty
T_1, T_2, T_3	0.06 °C
T_4	0.07 °C
T_{eo}	0.06 °C
T_{ci}	0.06 °C
T_{co}, T_{cci}	0.1 °C
T_{wa-i}	0.1 °C
T_{wa-o}	0.06 °C
Pressure transducer	1.5 kPa
Mass flow meter	0.18% of reading

**Figure 5.** Schematic design of the evaporator. 1: vapor collector; 2: compensation chamber; 3: polycarbonate lid; 4: O-ring; 5: charging pipe; 6: copper evaporator body; 7: wick; 8: vapor grooves; 9: copper plate; 10: vapor pipe.**Figure 6.** The inner surface geometry of the evaporator (a) before and (b) after installing the wick.

Furthermore, the experimental uncertainty analysis of the computed heat transfer coefficients is given by the following equation (Equations (4)–(13)).

The experimental result R is assumed to be calculated from a set of measurements using a data interpretation program presented by [21].

$$R = R(X_1, X_2, X_3, \dots, X_N) \quad (4)$$

Each measurement uncertainty's effect on the calculated result if only that one measurement were in error would be

$$\delta R_{X_i} = \frac{\partial R}{\partial X_i} \delta X_i \quad (5)$$

The partial derivative of R with respect to X_i is the sensitivity coefficient for result R with respect to measurement X_i . The single terms are combined by a root-sum-square method when respective independent variables are used in function R .

$$\delta R_{X_i} = \left\{ \sum_{i=1}^N \left(\frac{\partial R}{\partial X_i} \delta X_i \right)^2 \right\}^{\frac{1}{2}} \quad (6)$$

Then, the parameter ΔT_{12} can be defined as,

$$\Delta T_{12} = T_1 - T_2 \quad (7)$$

The uncertainty for ΔT_{12} is shown in Equation (8).

$$\delta(\Delta T_{12}) = \left(\delta T_1^2 + \delta T_2^2 \right)^{\frac{1}{2}} \quad (8)$$

where

ΔT_{12} is the temperature difference between T_1 and T_2 at the heating block.
The parameter ΔT_{23} can be defined as,

$$\Delta T_{23} = T_2 - T_3 \quad (9)$$

The uncertainty for ΔT_{23} is shown in Equation (10).

$$\delta(\Delta T_{23}) = \left(\delta T_2^2 + \delta T_3^2 \right)^{\frac{1}{2}} \quad (10)$$

where

ΔT_{23} is the temperature difference between T_2 and T_3 at the heating block.
The parameter ΔT_{13} can be defined as,

$$\Delta T_{13} = T_1 - T_3 \quad (11)$$

The uncertainty for ΔT_{13} is shown in Equation (12).

$$\delta(\Delta T_{13}) = \left(\delta T_1^2 + \delta T_3^2 \right)^{\frac{1}{2}} \quad (12)$$

where

ΔT_{13} is the temperature difference between T_1 and T_3 at the heating block.
The parameter q can be defined as,

$$q = k \frac{\Delta T_{12}}{\delta_1} \quad (13)$$

The uncertainty for q is shown in Equation (14).

$$\delta q = \frac{k}{\delta_1} \delta(\Delta T_{12}) \quad (14)$$

where

q is the heat flux; k is the thermal conductivity of copper.
 δ_1 is the distance between the heating block's thermocouples.
The parameter T_{bf} can be defined as,

$$T_{bf} = T_4 - \frac{q \delta_2}{k} \quad (15)$$

The uncertainty for T_{bf} is shown in Equation (16).

$$\delta(T_{bf}) = \left((\delta T_4)^2 + \left(\frac{\delta_2}{k} \delta q \right)^2 \right)^{\frac{1}{2}} \quad (16)$$

where

T_{bf} is the evaporator fin' base temperature.

T_4 is the evaporator's base temperature.

The parameter h_e can be defined as,

$$h_e = \frac{q}{T_{bf} - T_{eo}} \quad (17)$$

The uncertainty for h_e is shown in Equation (18).

$$\delta(h_e) = \left(\left(\frac{\delta q}{T_{bf} - T_{eo}} \right)^2 + \left(\frac{q \delta T_{eo}}{(T_{bf} - T_{eo})^2} \right)^2 + \left(\frac{q \delta T_{bf}}{(T_{bf} - T_{eo})^2} \right)^2 \right)^{\frac{1}{2}} \quad (18)$$

where

h_e is the heat transfer coefficient of the evaporator.

T_{eo} is the evaporator outlet temperature.

The parameter h_{esat} can be defined as,

$$h_{esat} = \frac{q}{T_{bf} - T_{esat}} \quad (19)$$

The uncertainty for h_{esat} is shown in Equation (20).

$$\delta(h_{esat}) = \left(\left(\frac{\delta q}{T_{bf} - T_{esat}} \right)^2 + \left(\frac{q \delta T_{esat}}{(T_{bf} - T_{esat})^2} \right)^2 + \left(\frac{q \delta T_{bf}}{(T_{bf} - T_{esat})^2} \right)^2 \right)^{\frac{1}{2}} \quad (20)$$

where

h_{esat} is the heat transfer coefficient of the evaporator, calculated from the saturation temperature.

T_{esat} is the saturation temperature accessed from vapor pressure.

2.2. Description of the Wick's Thermal Conductivity Measuring System

The wick materials' thermal conductivity was measured by the transient hot-wire method. Figure 7 shows a schematic diagram of the thermal conductivity measuring device and sensor unit. It consists of a power supply device, a measuring device, a sensor unit, and a recording device (Personal Computer, PC). At the time of measurement, a constant current is applied from the power supply to the sensor. In addition, the voltage drop of the sensor unit is measured by a measuring device at regular intervals and recorded by a recording device.

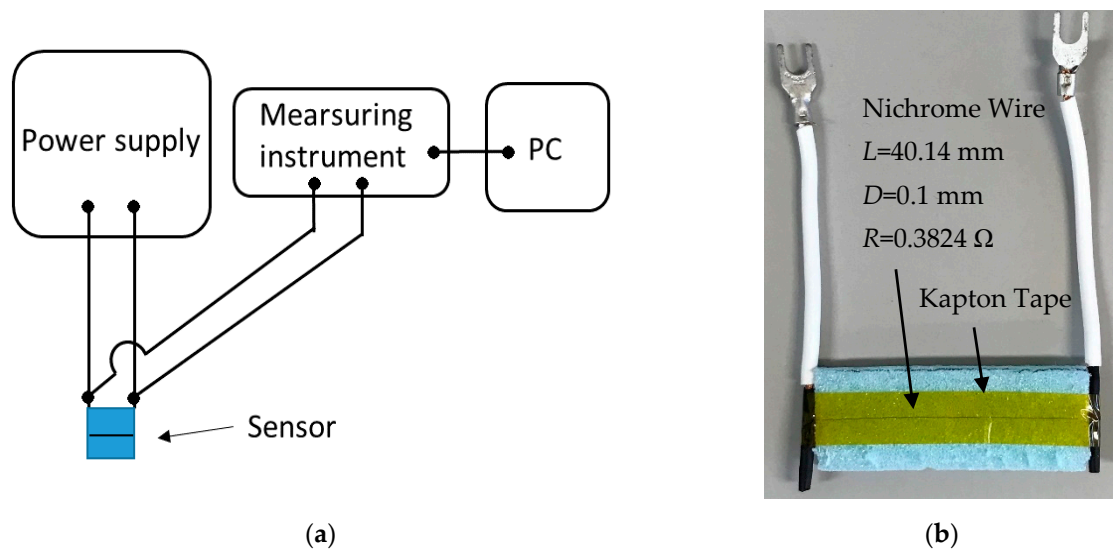


Figure 7. Thermal conductivity measuring device (a) Schematic Diagram (b) Sensor Unit.

The basic equation for thermal conductivity measurement is expressed by the following equations (Equations (21)–(24)).

The thermal conductivity of the wicks (Equation (21)) [22],

$$\lambda_2 = \frac{q^*}{2\pi} \frac{d \ln t}{d \Delta T} - \lambda_1 \quad (21)$$

where

λ_2 is the thermal conductivity of the wick sample.

λ_1 is the thermal conductivity of the insulator.

q^* is the amount of heating per wire length.

t is the time taken.

ΔT is the temperature change from $t = 0$ s.

Resistance of thin wire at a certain temperature,

$$R = R_0(1 + \alpha \Delta T) \quad (22)$$

where

R_0 is the initial electrical resistance.

α is the temperature coefficient of resistance.

From Equation (22) and Ohm's Law,

$$\Delta T = \frac{1}{\alpha} \left(\frac{V(t)}{IR_0} - 1 \right) \quad (23)$$

where

V is the voltage drop on the thin wire.

I is the current.

By substituting ΔT into Equation (21),

$$\frac{d V(t)}{d \ln t} = \frac{\alpha I^3 R_0^2}{2\pi(\lambda_1 + \lambda_2)} = \text{Constant} \quad (24)$$

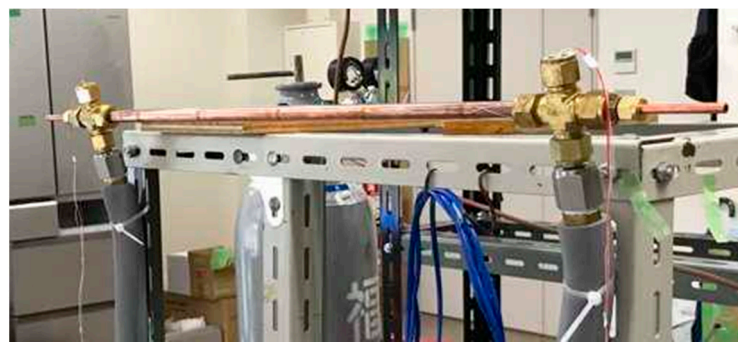
Then, the wick materials' thermal conductivity can be obtained from the slope of the relationship between the voltage drop of the thin wire and the logarithm of the heating time. The measured thermal conductivity of the tested wicks and the comparison with literature data [7,8] are presented in Table 5.

Table 5. Thermal conductivity of wicks.

Present Study		Value from References	
Wick	λ_2 [W (m K) ⁻¹]	Wick	λ_2 [W (m K) ⁻¹]
Stainless Steel	6.4	SP-Sintered [8]	11.87
Ceramic	3.5	Ceramic [7]	4

2.3. Description of Condenser

In this study, the condenser is a double-pipe heat exchanger with a counter flow arrangement. Cooling water from the constant temperature pump flows in the annular area while the vapor condenses inside the copper tube. The condenser structure is described in Figure 8 and Table 6.

**Figure 8.** Photograph of the condenser.**Table 6.** Specification of the condenser.

Parameters	Inner Tube	Outer Tube
Material	Smooth Copper tube	Poly-carbonated resin
Length, mm	600 mm	600 mm
OD/ID, mm	6.35/4.35	13/9

Furthermore, the same copper smooth tube is used for the vapor pipe and liquid pipe of the LHP, whose OD/ID is 6.35/4.35 and 3.2/1.5 mm, respectively.

2.4. Data Reduction

From Figure 3b, the values of heat flux q , heat transfer coefficient h_e , and thermal resistances R_e , R_c , and R_{ct} can be estimated by the following equations (Equations (25)–(36)): $A = 27 \text{ cm}^2$, $\delta_1 = 5 \text{ mm}$, $\delta_2 = 2.5 \text{ mm}$.

Heat flux flowing from the heating block to the evaporator's active area is calculated by Fourier's Law of heat conduction as

$$q' = k \frac{T_1 - T_2}{\delta_1} = k \frac{T_2 - T_3}{\delta_1} = k \frac{T_1 - T_3}{2\delta_1} \quad (25)$$

where

q' is the heat transfer rate per unit heating block's surface area.

k is the thermal conductivity of the copper heating block.

T_1 to T_3 is the heater temperature.

δ_1 is the distance between the thermocouples inside the heating block.

Then, the mean of q' can be expressed by Equation (26).

$$q = \frac{1}{3} \left(k \frac{\Delta T_{12}}{\delta_1} + k \frac{\Delta T_{23}}{\delta_1} + k \frac{\Delta T_{13}}{2\delta_1} \right) \quad (26)$$

$$Q = q * A \quad (27)$$

Additionally, the temperature of the heating block's top surface, T_{s1} , and the evaporator bottom's temperature, T_{s2} , can be determined by Equations (28) and (29).

$$T_{s1} = \frac{1}{3} \left[\left(T_1 - \frac{3(q\delta_1)}{k} \right) + \left(T_2 - \frac{2(q\delta_1)}{k} \right) + \left(T_3 - \frac{(q\delta_1)}{k} \right) \right] \quad (28)$$

$$T_{s2} = T_4 + \frac{q\delta_2}{k} \quad (29)$$

$$R_e = \frac{T_{s2} - T_{eo}}{Q} \quad (30)$$

$$R_c = \frac{T_{ci} - T_{wa-i}}{Q_c} \quad (31)$$

$$Q_c = m_{wa} C_p (T_{wa-o} - T_{wa-i}) \quad (32)$$

$$R_{ct} = \frac{T_{s1} - T_{s2}}{Q} \quad (33)$$

$$h_e = \frac{q}{T_{bf} - T_{eo}} \quad (34)$$

$$h_{esat} = \frac{q}{T_{bf} - T_{esat}} \quad (35)$$

$$T_{bf} = T_4 - \frac{q\delta_2}{k} \quad (36)$$

3. Results and Discussion

Figure 9 displays the values of temperature at various locations in the experiment. The results show that the stainless-steel wick exhibits higher heat flux when compared to the ceramic wick. During the heat load range of 50 to 520 W in Figure 9a and 53 to 155 W in Figure 9b, the values of T_{eo} and T_{ci} are almost similar, and T_{co} and T_{cci} are nearly equal. We affirm that the working fluid circulates stably inside the loop heat pipe. However, in the LHP with a ceramic wick, some fluctuations were found in the range of heat power, from 53 to 80 W, where the values of T_{cci} were higher than T_{co} . This phenomenon happened because there was the intermittent appearance of a vapor-liquid interface near the position of thermocouple T_{cci} in the liquid line. In the experiment of the LHP with a stainless steel wick, the supplying liquid for the compensation chamber was more stable than the LHP with the ceramic wick. Moreover, in this experimental research, temperature T_{s1} on the heating block's top surface can be viewed as the electronics temperature, which is normally recommended to be lower than 85 °C for reliable and effective operation [23]. Therefore, this present LHP, with stainless steel and ceramic wicks, can satisfy the recommendation until the heat load reaches 350 and 54 W, respectively. The measured values and frequency of pore distribution by the mercury injection method [24] are given in Table 7 and Figure 10.

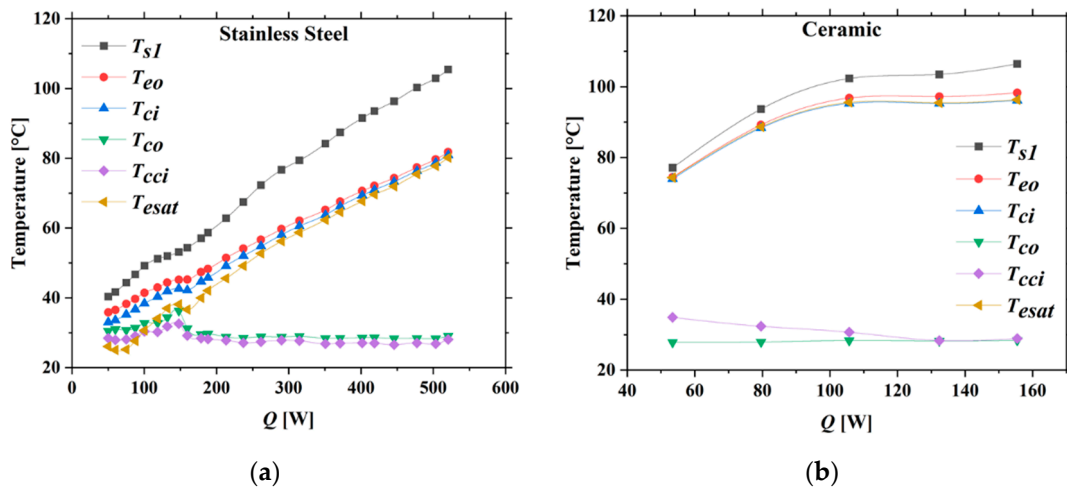


Figure 9. LHP’s temperatures distribution at different heat loads when installed with (a) a stainless-steel wick and (b) a ceramic wick.

Table 7. Test results of pore distribution measurement by the mercury injection method.

Wick Materials	Ceramic	Stainless Steel
Pore volume in total ($\text{cm}^3 \cdot \text{g}^{-1}$)	0.20	0.07
Central pore diameter (μm)	1.29	16.40
Total pore specific surface area ($\text{m}^2 \cdot \text{g}^{-1}$)	0.66	0.02
Average pore size (μm)	1.18	11.85
Bulk density ($\text{g} \cdot \text{cm}^{-3}$)	2.01	4.34
Porosity (%)	39.3	31.5

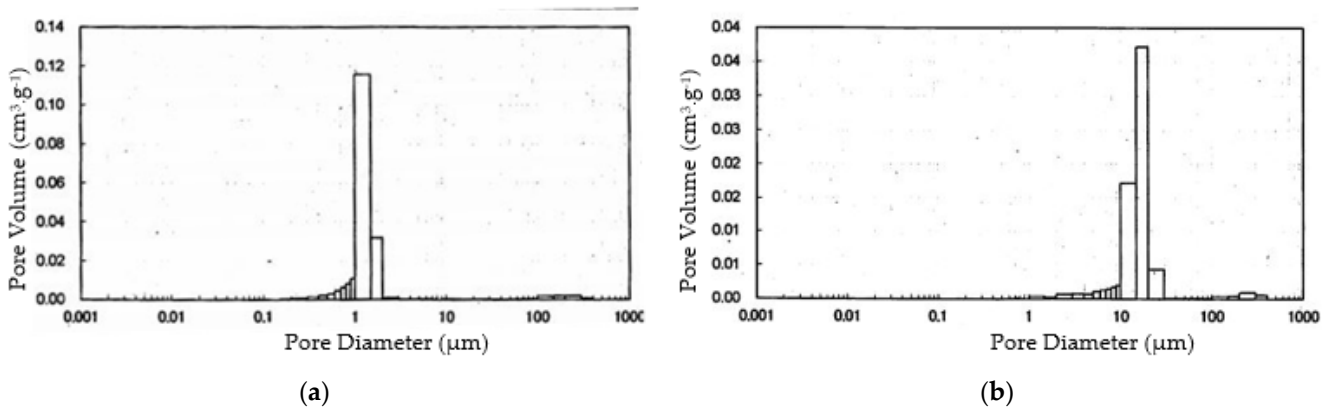


Figure 10. Pore frequency distribution graphs (a) Ceramic wick (b) Stainless steel wick. Reproduced from [25], Saga Ceramics Research Laboratory: 2019.

3.1. Performance Evaluation

The thermal performance can be evaluated in terms of heat flux q , heat transfer coefficient h_e , and thermal resistances, which are evaporator R_e , condenser R_c , and contact surface R_{ct} , as shown in Figures 11 and 12. In this study, the evaporator heat transfer coefficient was calculated from vapor temperature T_{eo} at the outlet of the evaporator and saturation temperature T_{esat} , accessed from the vapor pressure measured at the outlet of the evaporator.

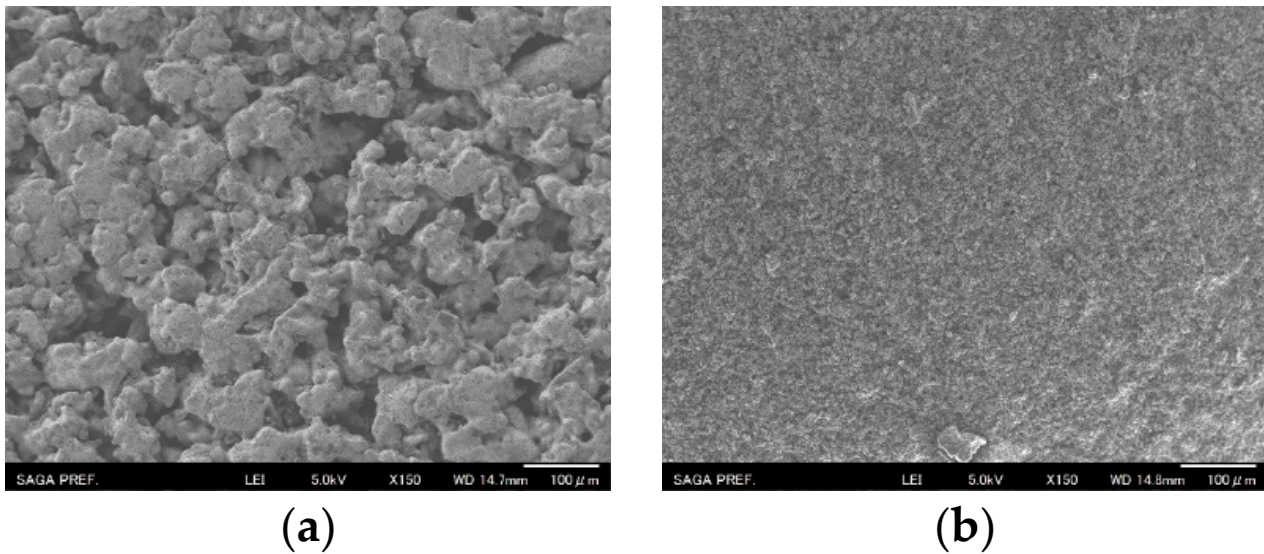


Figure 11. SEM images (100 μm magnification) of (a) a stainless steel wick and (b) a ceramic wick. Reproduced from [25], Saga Ceramics Research Laboratory: 2019.

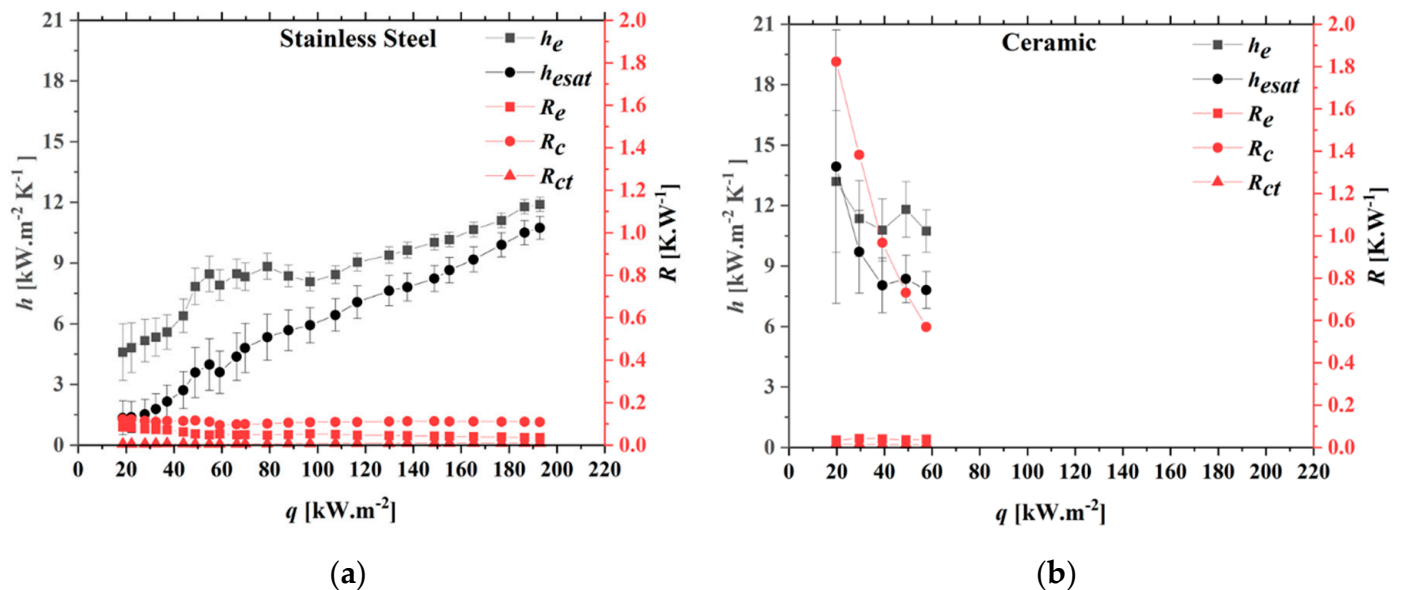


Figure 12. h_e , R , vs. q of (a) a stainless steel wick and (b) a ceramic wick.

In both experiments of stainless steel and ceramic LHPs, the evaporator heat transfer coefficient obtained from T_{eo} was higher than the values calculated from saturation temperature T_{esat} . Observing the difference in the results, the vapor might be superheated before leaving the evaporator. This superheating process could happen when vapor flows in the crossing grooves, and the heat of this process comes from the surrounding area of the fins and the grooves' surface. The possible operating heat flux for the stainless-steel wick was higher than the ceramic wick. Comparing the evaporator heat transfer coefficient of the LHPs, the evaporator operating with the ceramic wick had the higher evaporator heat transfer coefficient when the heat transfer coefficient, h_e , linearly increased with the heat flux in the LHP with the stainless steel wick. However, the ceramic LHP did not operate better than the stainless steel one. The significant mass flow rate of vapor requires large pore sizes in the ceramic wick to reduce resistance. Otherwise, the performance of the

condenser decreases. The numerical values obtained from the experimental uncertainty analysis of the computed heat transfer coefficients are presented in Tables 8 and 9.

Table 8. Uncertainty values of the computed heat transfer coefficients for LHPs with stainless steel wicks.

Q	q	$\delta(q)$	h_e	$\delta(h_e)$	h_{esat}	$\delta(h_{esat})$
W	W/m ²	%	W/(m ² ·K)	%	W/(m ² ·K)	%
50.22	18,598.44	30.42	4592.67	30.46	1345.93	62.64
100.29	37,299.05	15.17	5588.10	15.25	2150.30	37.71
147.91	54,451.96	10.39	8458.43	10.39	3984.10	32.14
188.17	69,832.60	8.10	8323.83	8.12	4804.16	25.30
237.16	87,723.91	6.45	8368.00	6.43	5676.28	17.73
290.03	107,645.92	5.26	8427.34	5.14	6428.54	12.52
350.72	129,896.27	4.35	9388.90	4.31	7633.87	9.80
401.67	148,767.07	3.80	10,023.39	3.77	8228.43	7.74
445.87	165,137.27	3.43	10,651.51	3.46	9177.51	6.74
503.47	186,469.50	3.03	11,785.25	3.08	10,499.12	5.67
520.70	192,826.71	2.93	11,900.59	2.99	10,742.33	5.26

Table 9. Uncertainty values of the computed heat transfer coefficients for LHPs with ceramic wicks.

Q	q	$\delta(q)$	h_e	$\delta(h_e)$	h_{esat}	$\delta(h_{esat})$
W	W/m ²	%	W/(m ² ·K)	%	W/(m ² ·K)	%
53.41	19,782.71	28.59	13,195.93	26.67	13,932.62	48.68
79.59	29,477.46	19.19	11,352.25	16.61	9709.18	21.12
105.72	39,154.18	14.45	10,783.11	14.27	8046.37	16.92
132.38	49,028.99	11.54	11,805.62	11.73	8359.43	14.03
155.45	57,574.38	9.83	10,737.34	9.87	7810.08	11.71

Performance of Evaporator and Condenser

Figure 12a,b displays the evaporator and condenser thermal resistances, R_e and R_c , of the stainless steel and ceramics LHPs. In the LHP with the stainless steel wick, the values of R_e became smaller with the increase in heating power. However, thermal resistance R_e for the ceramic one gradually increased in the same operating conditions, although the performance of the evaporator with the ceramic wick was more effective than the one with the stainless steel wick. For the thermal resistances of the condenser at the stainless steel LHP, it was reduced to the minimum value of 0.09 K.W⁻¹, then raised up slightly, as shown in Figure 12a. The higher the heat power supplied to the evaporator, the less liquid exists inside the compensation chamber. As a result, with more liquid present in the condenser with the increasing heat load, the performance of the condenser was slightly reduced.

For the LHP with the ceramic wick, R_c 's values were significantly high, i.e., 1.8 K.W⁻¹ at 53 W, due to the lower performance of the condenser. Additionally, particle differences between the stainless steel wick and ceramic wick are apparent in Figure 11a,b; the interfaces between the particles in Figure 11b are not as straightforward as those in Figure 11a. In the loop heat pipe with the stainless-steel wick, the working fluid was smoothly circulating inside the LHP because the flow resistance through the stainless-steel wick was lower than that of the ceramic wick. Therefore, the heat supplied made the working fluid evaporate, and the heat leak through the stainless-steel wick became small. In the ceramic wick's case, the working fluid was not able to circulate correctly inside the LHP due to the high hydraulic resistance in the ceramic wick. As a result, heat flow, called a heat leak, became dominant in the evaporator with the ceramic wick.

4. Conclusions

The influence of two different wicks was tested in this study and used to describe the LHPs' performance with a flat rectangular evaporator. The experimental results demonstrate that the LHP with the stainless-steel wick has better cooling performance than the LHP with the ceramic wick. The heater surface temperature of the LHP with the stainless steel wick increased from 40 to 105 °C in the range of a heat load from 50 to 520 W. In the ceramic wick LHP, this surface temperature reached 106 °C at a heat load of 155 W. Under gravity-assisted conditions, the LHP with the stainless steel wick could keep the temperature on the heater surface at 85 °C for a heat load of 350 W. However, the LHP with the ceramic wick could operate only at lower than 118 W for the same LHP, and the heater's surface temperature approached 85 °C when the LHP was conducted at 54 W (20 kW·m⁻²). The ceramic wick cannot handle a high heat flux because of the conflict between vapor release and liquid suction. Large pore sizes are required to reduce resistance for the significant mass flow rate of vapor. It has been explained by Meléndez and Reyes [26].

$$m_v = \frac{\pi}{128} \left(\frac{\rho_v \sigma}{\mu_v} \right) \left(\frac{\varepsilon d_e^3}{d} \right) \quad (37)$$

where

m_v is the vapor mass flow rate; ρ_v , σ , μ_v , and ε are vapor density, surface tension, viscosity, and porosity, respectively; δ is the wick thickness, and d_e is the effective pore diameter.

On the other hand, large capillary pressure is achieved by tiny pores for liquid suction, according to the Laplace-Young equation.

$$\Delta P = \frac{4\sigma \cos \alpha}{d_e}, \quad \alpha \text{ is the contact angle} \quad (38)$$

As a result, the vapor release and liquid suction of the ceramic wick require different pore sizes for better heat performance in LHPs.

Author Contributions: Conceptualization, A.M. and K.K.; methodology, A.M., K.K. and P.H.H.; software, P.H.H. and K.Z.H.; validation, P.H.H. and K.Z.H.; formal analysis, P.H.H. and K.Z.H.; investigation, P.H.H. and K.Z.H.; resources, A.M. and K.K.; data curation, P.H.H. and K.Z.H.; writing—original draft preparation, K.Z.H.; writing—review and editing, K.Z.H. and A.M.; visualization, P.H.H. and K.Z.H.; supervision, A.M.; project administration, A.M. and K.K.; funding acquisition, A.M. and K.K. All authors have read and agreed to the published version of the manuscript.

Funding: This research received no external funding.

Institutional Review Board Statement: Not applicable.

Informed Consent Statement: Not applicable.

Data Availability Statement: Not applicable.

Conflicts of Interest: The authors declare no conflict of interest.

Nomenclature

T_{s1}	temperature at heater surface ($^{\circ}\text{C}$)	T_{bf}	fin base temperature ($^{\circ}\text{C}$)
ID, OD	pipe inner/outer diameter (mm)	T_{ci}	condenser inlet temperature ($^{\circ}\text{C}$)
k	thermal conductivity of copper heating block [$\text{W}\cdot(\text{m K})^{-1}$]	T_{co}	condenser outlet temperature ($^{\circ}\text{C}$)
q	heat flux ($\text{kW}\cdot\text{m}^{-2}$)	T_{cci}	compensation chamber inlet temperature ($^{\circ}\text{C}$)
Q	heat load (W)	T_{eo}	evaporator outlet temperature ($^{\circ}\text{C}$)
R_e	thermal resistance of evaporator ($\text{K}\cdot\text{W}^{-1}$)	T_{s2}	evaporator bottom surface temperature ($^{\circ}\text{C}$)
R_c	thermal resistance of condenser ($\text{K}\cdot\text{W}^{-1}$)	T_{wa-i}	cooling water temperature at inlet position ($^{\circ}\text{C}$)
R_{ct}	thermal contact resistance ($\text{K}\cdot\text{W}^{-1}$)	T_{wa-o}	cooling water temperature at outlet position ($^{\circ}\text{C}$)
T_1 to T_3	heater temperature ($^{\circ}\text{C}$)	δ_1	distance between the thermocouples inside heating block (m)
T_4	evaporator base temperature ($^{\circ}\text{C}$)	δ_2	distance between the thermocouple T_4 and the bottom surface of evaporator (m)
Q_c	heat released from condenser (W)	C_p	specific heat of cooling water [$\text{J}\cdot(\text{kg K})^{-1}$]
m_{wa}	mass flow rate of cooling water ($\text{kg}\cdot\text{s}^{-1}$)	T_{esat}	saturation temperature accessed from vapor pressure
h_e	heat transfer coefficient of evaporator ($\text{kW}\cdot\text{m}^{-2}\text{K}^{-1}$)	h_{esat}	evaporator heat transfer coefficient calculated from saturation temperature ($\text{kW}\cdot\text{m}^{-2}\text{K}^{-1}$)
ΔT	temperature change from $t = 0$ ($^{\circ}\text{C}$)	t	time (s)
q^*	amount of heating per wire length ($\text{W}\cdot\text{m}^{-1}$)	T_o	initial temperature ($^{\circ}\text{C}$)
R_o	initial electrical resistance (Ω)	α	temperature coefficient of resistance ($^{\circ}\text{C}^{-1}$)
V	voltage drop on thin wire (V)	L	thin wire length (mm)
A	area of heating block surface (m^2)	λ_2	thermal conductivity of wick sample [$\text{W}\cdot(\text{m K})^{-1}$]
I	electric current (I)	λ_1	thermal conductivity of insulator [$\text{W}\cdot(\text{m K})^{-1}$]
q	heat transfer rate per unit heating block's surface area ($\text{kW}\cdot\text{m}^{-2}$)		

References

- Maydanik, Y.F. Loop heat pipes. *Appl. Therm. Eng.* **2005**, *25*, 635–657. [\[CrossRef\]](#)
- Zhou, W.; Ling, W.; Duan, L.; Hui, K. Development and tests of loop heat pipe with multi-layer metal foams as wick structure. *Appl. Therm. Eng.* **2016**, *94*, 324–330. [\[CrossRef\]](#)
- Siedel, B.; Sartre, V.; Lefèvre, F. Numerical investigation of the thermo hydraulic behaviour of a complete loop heat pipe. *Appl. Therm. Eng.* **2013**, *61*, 541–553. [\[CrossRef\]](#)
- Maydanik, Y.; Fershtater, Y.G.; Pastukhov, V.G. *Loop Heat Pipes: Development, Investigation and Elements of Engineering Calculations*; Technical Report; Ural Division of the USSR Academy of Sciences: Moscow, Russia, 1989.
- Hoang, T.T.; O'Connell, T.A.; Ku, J.; Butler, C.D.; Swanson, T.D. Miniature loop heat pipes for electronic cooling. In Proceedings of the ASME 2003 International Electronic Packaging Technical Conference and Exhibition, Maui, HI, USA, 6–11 July 2003; pp. 517–525.
- Kondou, C.; Umemoto, S.; Koyama, S.; Mitooka, Y. Improving the heat dissipation performance of a looped thermosyphon using low-GWP volatile fluids R1234ze(Z) and R1234ze(E) with a super-hydrophilic boiling surface. *Appl. Therm. Eng.* **2017**, *118*, 147–158. [\[CrossRef\]](#)
- Santos, P.H.; Bazzo, E.; Becker, S.; Kulenovic, R.; Mertz, R. Development of LHPs with ceramic wick. *Appl. Therm. Eng.* **2010**, *30*, 1784–1789. [\[CrossRef\]](#)
- Canti, G.; Celata, G.P.; Cumo, M.; Furrer, M. Thermal hydraulic characterization of stainless steel wicks for heat pipe applications. *Rev. Gén. Therm.* **1998**, *37*, 5–16. [\[CrossRef\]](#)
- Ji, X.; Wang, Y.; Xu, J.; Huang, Y. Experimental study of heat transfer and start-up of loop heat pipe with multiscale porous wicks. *Appl. Therm. Eng.* **2017**, *117*, 782–798. [\[CrossRef\]](#)
- Maydanik, Y.; Chernysheva, M.; Pastukhov, V.G. Review: Loop heat pipes with flat evaporators. *Appl. Therm. Eng.* **2014**, *67*, 294–307. [\[CrossRef\]](#)
- Fukushima, K.; Nagano, H. International Journal of Heat and Mass Transfer New evaporator structure for micro loop heat pipes. *Int. J. Heat Mass Transf.* **2017**, *106*, 1327–1334. [\[CrossRef\]](#)
- Nishikawara, M.; Nagano, H. International Journal of Heat and Mass Transfer Optimization of wick shape in a loop heat pipe for high heat transfer. *Int. J. Heat Mass Transf.* **2017**, *104*, 1083–1089. [\[CrossRef\]](#)

13. Xu, J.; Ji, X.; Yang, W.; Zhao, Z. Modulated porous wick evaporator for loop heat pipes: Experiment. *Int. J. Heat Mass Transf.* **2014**, *72*, 163–176. [[CrossRef](#)]
14. Wu, S.; Wang, D.; Gao, J.; Huang, Z.; Chen, Y. Effect of the number of grooves on a wick's surface on the heat transfer performance of loop heat pipe. *Appl. Therm. Eng.* **2014**, *71*, 371–377. [[CrossRef](#)]
15. Choi, J.; Sung, B.; Kim, C.; Borca-Tasciuc, D.-A. Interface engineering to enhance thermal contact conductance of evaporators in miniature loop heat pipe systems. *Appl. Therm. Eng.* **2013**, *60*, 371–378. [[CrossRef](#)]
16. Singh, R.; Akbarzadeh, A.; Mochizuki, M. Operational characteristics of a miniature loop heat pipe with flat evaporator. *Int. J. Therm. Sci.* **2008**, *47*, 1504–1515. [[CrossRef](#)]
17. Chernysheva, M.; Yushakova, S.; Maydanik, Y. Copper–water loop heat pipes for energy-efficient cooling systems of supercomputers. *Energy* **2014**, *69*, 534–542. [[CrossRef](#)]
18. Zhou, G.; Li, J.; Lv, L. An ultra-thin miniature loop heat pipe cooler for mobile electronics. *Appl. Therm. Eng.* **2016**, *109*, 514–523. [[CrossRef](#)]
19. Shioga, T.; Mizuno, Y. Micro loop heat pipe for mobile electronics applications. In Proceedings of the 2015 31st Thermal Measurement, Modeling & Management Symposium (SEMI-THERM), San Jose, CA, USA, 15–19 March 2015; pp. 50–55.
20. Li, J.; Lin, F.; Wang, D.; Tian, W. A loop-heat-pipe heat sink with parallel condensers for high-power integrated LED chips. *Appl. Therm. Eng.* **2013**, *56*, 18–26. [[CrossRef](#)]
21. Moffat, R.J. Describing the uncertainties in experimental results. *Exp. Therm. Fluid Sci.* **1988**, *1*, 3–17. [[CrossRef](#)]
22. Takekoshi, E.; Imura, S.; Hirasawa, Y.; Takenaka, T. *Method for Measuring Thermal Conductivity of Solids by Transient Thin Wire heating Comparison Method (Edition. B)*; Japan Society of Mechanical Engineers: Tokyo, Japan, 1981; Volume 47, pp. 1307–1316. [[CrossRef](#)]
23. Ebrahimi, K.; Jones, G.F.; Fleischer, A.S. A review of data center cooling technology, operating conditions and the corresponding low-grade waste heat recovery opportunities. *Renew. Sustain. Energy Rev.* **2014**, *31*, 622–638. [[CrossRef](#)]
24. Nourzadeh, N.; Shadizadeh, S.R.; Manshad, A.K. Determination of pore size distribution profile along wellbore: Using repeat formation tester. *J. Pet. Explor. Prod. Technol.* **2017**, *7*, 621–626. [[CrossRef](#)]
25. Saga Ceramics Research Laboratory. Available online: <https://www.scrl.gr.jp/main/> (accessed on 28 November 2019).
26. Meléndez, E.; Reyes, R. The pool boiling heat transfer enhancement from experiments with binary mixtures and porous heating covers. *Exp. Therm. Fluid Sci.* **2006**, *30*, 185–192. [[CrossRef](#)]